Interplanetary Hydrogen Properties Observed from Mars

M. Mayyasi, Eric Quémerais, Dimitra Koutroumpa, I. Baliukin, A. Titova, V. Izmodenov, J. Clarke, J. Deighan, N. Schneider, S. Curry

JGR Space Physics

RESEARCH ARTICLE
10.1029/2023JA031447

Interplanetary Hydrogen Properties Observed From Mars

M. Mayyasi[1], E. Quémerais[2], D. Koutroumpa[2], I. Baliukin[3,4,5], A. Titova[3,5], V. Izmodenov[3,4], J. Clarke[6], J. Deighan[7], N. Schneider[7], and S. Curry[8]

[1]Center for Space Physics, Boston University, Boston, MA, USA, [2]LATMOS-OVSQ, Université Versailles Saint-Quentin, Guyancourt, France, [3]Space Research Institute (IKI) of Russian Academy of Sciences, Moscow, Russia, [4]Moscow Center for Fundamental and Applied Mathematics, Lomonosov Moscow State University, Moscow, Russia, [5]HSE University, Moscow, Russia, [6]Astronomy Department, Boston University, Boston, MA, USA, [7]Laboratory for Atmospheric and Space Physics, University of Colorado Boulder, Boulder, CO, USA, [8]Space Sciences Laboratory, University of California, Berkeley, CA, USA

Key Points:

- Interplanetary Hydrogen (IPH) Lyman-a brightness trends with solar irradiance with fainter flow downwind than upwind
- IPH Lyman-a brightness is variable and non-negligible when viewed from Mars-orbiting spacecraft
- MAVEN IPH observations can be used to constrain the inner boundary conditions of heliospheric models

Correspondence to:
M. Mayyasi,
majdm@bu.edu

Citation:
Mayyasi, M., Quémerais, E., Koutroumpa, D., Baliukin, I., Titova, A., Izmodenov, V., et al. (2023). Interplanetary hydrogen properties observed from Mars. *Journal of Geophysical Research: Space Physics*, *128*, e2023JA031447. https://doi.org/10.1029/2023JA031447

Received 27 FEB 2023
Accepted 26 MAY 2023

Author Contributions:

Conceptualization: M. Mayyasi
Data curation: M. Mayyasi, J. Deighan
Formal analysis: M. Mayyasi
Funding acquisition: J. Clarke, N. Schneider
Investigation: M. Mayyasi
Methodology: M. Mayyasi, E. Quémerais
Project Administration: M. Mayyasi
Software: M. Mayyasi, D. Koutroumpa, I. Baliukin, A. Titova, V. Izmodenov
Validation: M. Mayyasi, E. Quémerais, I. Baliukin, A. Titova, V. Izmodenov
Visualization: M. Mayyasi
Writing – original draft: M. Mayyasi
Writing – review & editing: M. Mayyasi, E. Quémerais, I. Baliukin, J. Clarke

Abstract Observations of the Lyman-α emissions from Interplanetary Hydrogen (IPH) atoms are made from Mars' orbit using a high spectral resolution instrument in echelle configuration. The measurements can uniquely be used to resolve IPH from planetary H emissions and to subsequently determine the brightness, velocity, and thermal broadening of the IPH flow along the instrument line of sight. Planned observations conducted during special IPH campaigns as well as serendipitous observations made of the planetary limb and a comet sighting, both upwind and downwind of the bulk IPH flow direction, are analyzed to determine these properties and to examine the variability of IPH brightness with solar activity through the declining phase of Solar Cycle 24. The results show that the IPH brightness trends with solar irradiance, the flow is fainter downwind than upwind, the IPH brightness is variable and non-negligible compared with planetary emissions, and that deriving thermal properties of IPH requires higher spectral resolution than is presently available. A heliospheric interface model was used to simulate and further interpret the derived IPH properties. These results can improve the theoretical understanding of solar system dynamics, between the solar wind and the local interstellar medium, by providing empirical constraints to simulations of the global heliosphere from the inner boundary region near 1.6 AU and can guide the development of future interplanetary missions.

1. Background

The motion of the solar system through the local interstellar medium (LISM) carves out a cavity around the Sun known as the heliosphere. Neutral H atoms populate the heliosphere, and these atoms originate from the solar wind, the interstellar medium, as well as from processes that neutralize protons via charge exchange throughout the region (Bertaux & Blamont, 1971; Lallement et al., 1993; Thomas & Krassa, 1971; Quémerais, Lallement, Bertaux, et al., 2006 and references therein). The collective population of these neutral H atoms through the solar system is called Interplanetary Hydrogen (IPH). The effects of the Sun on the IPH flow, such as radiation pressure and gravitational forces are strongest near the Sun and fall off as the square of the distance such that within a few AUs from the Sun, the solar wind ionizing power creates a void of neutral H atoms (McComas et al., 2004; Quémerais et al., 2014; Kowalska-Leszczynska et al., 2018).

H atoms resonantly scatter Lyman-α photons. IPH properties have therefore been examined using Lyman-α emissions observed by multiple spacecraft from various points in the solar system (e.g., Baliukin et al., 2022; Galli et al., 2022; Zank et al., 2022) It is found that the IPH flow direction emanates from close to the heliospheric "nose" with no significant variation of the IPH flow longitude over time (Lallement et al., 2005; Koutroumpa et al., 2017). The IPH velocity ranges between 18 ± 2 km/s and 25.7 ± 2 km/s, and varies with solar activity, line of sight, and distance from the Sun (Vincent et al., 2011). The abundance, velocity, and thermal distribution of these atoms vary over solar cycle timescales and have been used to determine how the Sun and the LISM interact (e.g., Quémerais, Lallement, Ferron, et al., 2006; Katushkina et al., 2019, 2021).

The Solar and Heliospheric Observatory (SOHO) spacecraft has a Solar Wind Anisotropy (SWAN) photometer that includes a hydrogen cell used to measure Lyman-α intensity (Bertaux et al., 1995). For decades, SWAN measurements have been used to determine the distribution of IPH atoms, compare this distribution with models to obtain the heliographic distribution of ionizing flux from the Sun, and to derive the spatial and temporal variations of solar wind mass flux (Bertaux et al., 1995, 1997; Quémerais et al., 1999). SWAN has been in operation

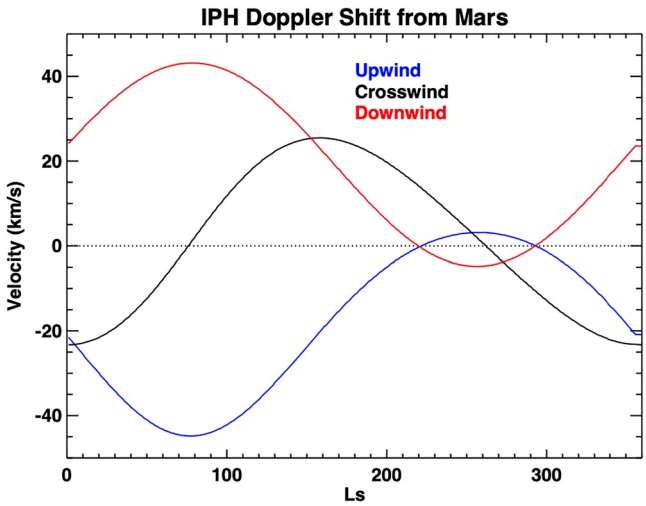

Figure 1. The Doppler shift of the IPH flow along the line of sight from Mars as a function of the planet's orbital location, denoted by solar longitude (Ls) in degrees. Looking upwind (blue), crosswind (black), and downwind (red) to the IPH flow results in a variable Doppler shift throughout Mars' orbital path. A horizontal dotted black line is shown at 0 km/s for reference.

at the L1 Lagrange point since 1996 (the beginning of Solar Cycle 23) and has shown some degradation. It is therefore opportune for other instruments to supplement the valuable SWAN data set with some continuity.

In this work, seven years (2014–2021) of observations obtained from ∼1.6 AU (Mars' orbit at its aphelion) were examined to derive IPH properties over the relatively moderate Solar Cycle 24's declining phase. The IPH upwind direction is at ecliptic longitude and latitude of 252.5° and 8.9°, respectively (Lallement et al., 2010). The downwind direction is at ecliptic longitude and latitude of 72.5° and −8.9°, respectively. MAVEN observations along the upwind flow direction as well as downwind to the flow were analyzed and compared. A model simulating the heliospheric interface was used for comparison (Izmodenov & Alexashov, 2015, 2020). The results from this analysis can empirically constrain IPH models at 1.6 AU, where few IPH measurements have been made, and can refine our understanding of how the solar system interacts with the LISM in the dynamic heliosphere (e.g., Izmodenov, 2007; Vincent et al., 2014).

2. Observations

The Mars Atmosphere and Volatile Evolution (MAVEN) spacecraft has been in orbit since September 2014, carrying an instrument suite that includes an Imaging Ultraviolet Spectrograph (IUVS) with a high-spectral resolution echelle component (McClintock et al., 2014; Jakosky et al., 2105; Mayyasi et al., 2023). The high spectral-resolution capabilities were designed to resolve hydrogen and deuterium (D) Lyman-α emissions at 121.567 and 121.534 nm, respectively (e.g., Mayyasi, Clarke, Bhattacharyya, et al., 2017; Mayyasi, Clarke, et al., 2019). The optical design of IUVS/Echelle can also resolve planetary H from IPH Lyman-α emissions at times when there is sufficient Doppler shift between the two H populations along the instrument line of sight.

Once a spectrally resolved IPH emission spectrum is obtained, the data can be used to derive brightness, velocity, and thermal broadening of the IPH flow along the line of sight (Mayyasi, Clarke, Quémerais, et al., 2017). Since both upwind and downwind observations are available, an additional useful diagnostic to derive is the variability in upwind to downwind properties of the IPH flow using observations made close in time. This diagnostic would be useful for interpreting IPH flow dynamics in the inner heliosphere (Clarke et al., 1998). A unique feature of this data set is the availability of both upwind as well as downwind IPH observations obtained in the same epoch.

The MAVEN IUVS instrument makes routine observations of IPH to calibrate the spectrograph as well as to monitor for possible signs of degradation in the instrument (Mayyasi, Clarke, Quémerais, et al., 2017). During a few months in each Mars Year (MY), typically around aphelion when the Solar longitude (Ls) is less than 180°, the velocity of Mars along its orbit (∼24 km/s) produces a maximum Doppler shift with the IPH flow, as shown in Figure 1. The upwind IPH direction is at RA and DEC of 16.8^{h} and −13.5°, respectively. The downwind IPH direction is at an RA and DEC of 4.8^{h} and 13.5°, respectively. The crosswind IPH direction is at an RA and DEC of 10.8^{h} and 6.9°, respectively. We adopt an average IPH velocity of ∼23.3 km/s relative to the Sun, resulting in a maximum Doppler shift of ∼±44 km/s at ∼78° Ls when looking upwind/downwind to the IPH flow from Mars.

The IUVS/ECH line spread function has a full-width-half-max (FWHM) of ∼17.5 km/s. Therefore, a filter of at least 2 × FWHM (∼35 km/s) was considered optimal for detecting and analyzing IPH properties in the IUVS/ECH limb scans. These detections do not overlap with planetary D Lyman-α emissions, that are separated from the Mars at-rest H wavelength by over 6 × FWHM, and interstellar D emissions are too faint to be detectable above the IUVS background (e.g., Solomon & Woolf, 1973; Rodríguez Moreno et al., 2013). Due to this selection criterion, observations where the line of sight was crosswind to the IPH flow had Doppler shifts (peaking at ±25 km/s) are too small to spectrally resolve the IPH feature and are therefore not analyzed in this work.

During the optimally Doppler shifted upwind conditions, MAVEN conducted planned IPH observing campaigns. In December 2019, interstellar Comet 2I/Borisov was making its closest approach at a time when MAVEN/IUVS had favorable viewing geometry. The line of sight to the comet serendipitously captured an optimally Doppler shifted downwind IPH flow. Two upwind campaign observations were measured at −28 km/s (in MY 34) and at

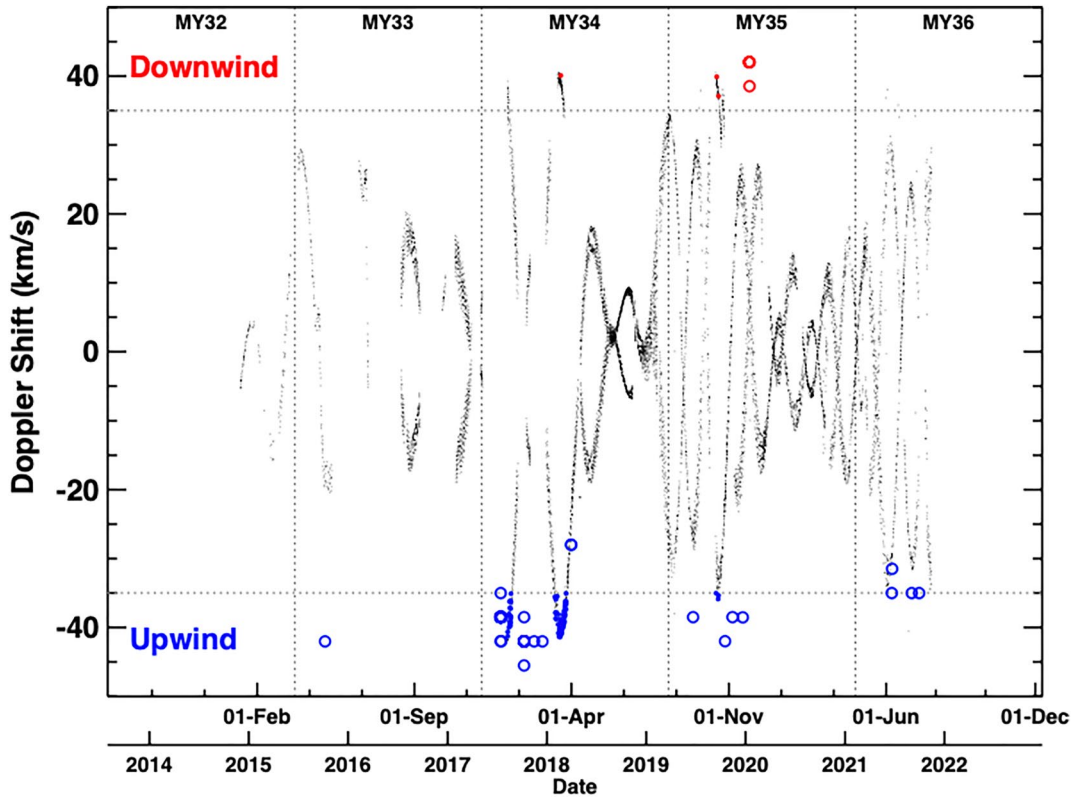

Figure 2. MAVEN IUVS timeline of Doppler shift from all limb-scans (dots) and dedicated IPH campaign (open circles). Horizontal black dotted lines denote the spectral resolvability limit for IPH emissions for limb observations at ±35 km/s. This criterion results in 88 data points (solid circles) available from fortuitous limb pointing in addition to the 37 campaign observations. Upwind observations used in this analysis are in blue (negative Doppler shifts) and downwind observations are in red (positive Doppler shifts). The downwind campaign observations (red open circles) were obtained during Comet 2I/Borisov's closest approach.

−31 km/s (in MY 36) and are useable due to the faintness of Mars planetary emissions along the line of sight. The remaining upwind and downwind campaign observations were at Doppler shifts beyond ±35 km/s. In addition to IPH campaign observations, nominal science observations have been found to fortuitously have a resolvable IPH component when the instrument line of sight is pointed off the planetary disk and through the limb. The observations analyzed in this work, relative to the available archive of observations, are highlighted in Figure 2 and listed in Appendix A.

Between November 2014 and November 2021, a total of 125 observations were found to be suitable for resolving the IPH emission to derive the properties of the flow. Of these useable observations, 37 are obtained from dedicated IPH campaigns, and 88 are from limb scans. Of the dedicated IPH campaign data points, 33 were made upwind of the IPH flow, and 4 were made downwind. Of the 88 limb scans, 85 were upwind and 3 were downwind of the IPH flow.

From a scientific perspective, the campaign data differ from limb observations in that they were planned to point away from the planet and/or at a comet rather than close to the Martian disk. The IPH emission, that is the focus of this study, is diffuse and appears in all off-planet data. There is therefore no bias in the IPH emissions obtained in the MAVEN/IUVS echelle limb or campaign observations. From an operational perspective, the echelle data obtained for IPH campaign versus limb scans differ in the region of the 1024 × 1024 detector that is used to bin and download the data (e.g., Table A1 in Mayyasi, Clarke, Quémerais, et al., 2017). The spectral binning is consistent for all echelle mode data in the IUVS data set, and accommodations for different spatial binning schemes has been done prior to this analysis with an updated calibration and data-reduction pipeline (Mayyasi et al., 2023). The resulting spectra are consistent and can be co-analyzed and compared across various IUVS echelle observing modes and lines of sight.

The IUVS/ECH data, obtained from both the dedicated IPH campaigns as well as limb scan observations have between 20 and 60 frames (images) per orbit. A single frame consists of a 29 s exposure for limb scans, and a 60 s exposure for campaign observations. During the integration time for each orbit in the observations used here, the IPH flow direction does not vary significantly. Subsequently, the IPH Lyman-α emission count rate, peak wavelength, and width (that are collectively used to derive brightness, Doppler shift, and temperature) also do not vary significantly from frame to frame in the spectra obtained from a single MAVEN orbit. Frames from each orbit are therefore averaged to produce a single spectrum to optimize the signal to noise ratio (e.g., Mayyasi et al., 2023).

3. Method

The MAVEN spacecraft orbits within the extended Mars H corona. Therefore, all Lyman-α observations made along the IUVS/ECH line of sight include a planetary H emission component. Sample spectra including Mars H, IPH, and for limb data, Mars D, emissions and their best fits are shown in Figure 3 for observations made during upwind/downwind campaigns as well as upwind/downwind limb scans.

To resolve each emission and derive the IPH properties, minimum variance analysis was used. First estimates of the (a) planetary at-rest H emission peak wavelength, (b) Doppler shifted IPH emission peak wavelength, (c) thermal broadening of the IPH emission, (d) percentage of thermal H contribution to the total Lyman-α emission, and (e) percentage of IPH contribution to the total Lyman-α emission are derived from the spacecraft ephemeris and literature adopted values. An iterative algorithm was then run that varied the first estimates within set ranges and generated a spectrum for each combination of the five parameters. The modeled spectrum was compared with the data and a matrix of χ^2 values was generated for each combination of the parameters. The parameter set that produced the minimum χ^2 value was used to generate the best-fit curve, as shown in Figure 3. The resulting best fit curve for each of the 125 spectra was examined by eye to confirm accurate representation of the data.

The first estimate for at-rest emission peak wavelength for Mars H is 121.567 nm. The first estimate for emission peak wavelength of IPH was derived from the line of sight geometry that accounted for the velocity of Mars, MAVEN, and the IPH flow along the instrument line of sight. The range of velocities for each emission peak used in the fitting algorithm were $\pm 0.2 \times$ FWHM of their first estimates, varied in $0.1 \times$ FWHM increments, to account for minimal velocity changes due to the motion of the MAVEN spacecraft around Mars (~2.5 km/s) as well as for the IUVS/ECH spectral resolution (~3.5 km/s/binned pixel (Mayyasi, Clarke, Quémerais, et al., 2017)).

Mars H atoms are typically thermalized at ~200–350 K (Mayyasi et al., 2022c). These temperatures do not significantly broaden the planetary emission line profile beyond a characteristic shape, empirically determined by the instrument line spread function (LSF) (Mayyasi et al., 2023). IPH atoms are typically several thousands of degrees K, resulting in a thermally broadened Lyman-α emission profile (Wu & Judge, 1980; Bertaux et al., 1985; Clarke et al., 1998; Mayyasi, Clarke, Quémerais, et al., 2017). An optimal line shape to use for IPH emission line profile fits was obtained by convolving the instrument LSF with a Voigt profile of some temperature (LSF⊗Voigt). The IPH temperature range considered here was between 11,000 K and 15,000 K, varied in 500 K increments.

The smaller the Doppler shift of the IPH flow along the instrument line of sight, the closer the overlap between Mars H and IPH emissions. The fluxes of the Mars H peak emission and that of the IPH emission, at the assumed Doppler shift were used as first estimates to constrain the fits of the emission line shapes generated by the fitting algorithm. These peak fluxes were then varied by ±10% in 2% increments in the iterations to obtain an optimal fit to the data.

Using this methodology, described in more detail in Appendix A, the best fit spectra generated for IPH and Mars H emissions were integrated across wavelength to derive brightness (e.g., Mayyasi et al., 2023). The IPH temperature and velocity, along the line of sight, were obtained from the remaining best fit parameters directly.

4. Results

4.1. Spatial Distribution

The distribution of the observations relative to the IPH upwind and downwind directions is shown in Figure 4. The IPH upwind campaign observations deviated from the upwind flow direction by anywhere from ~3° to 60°, with

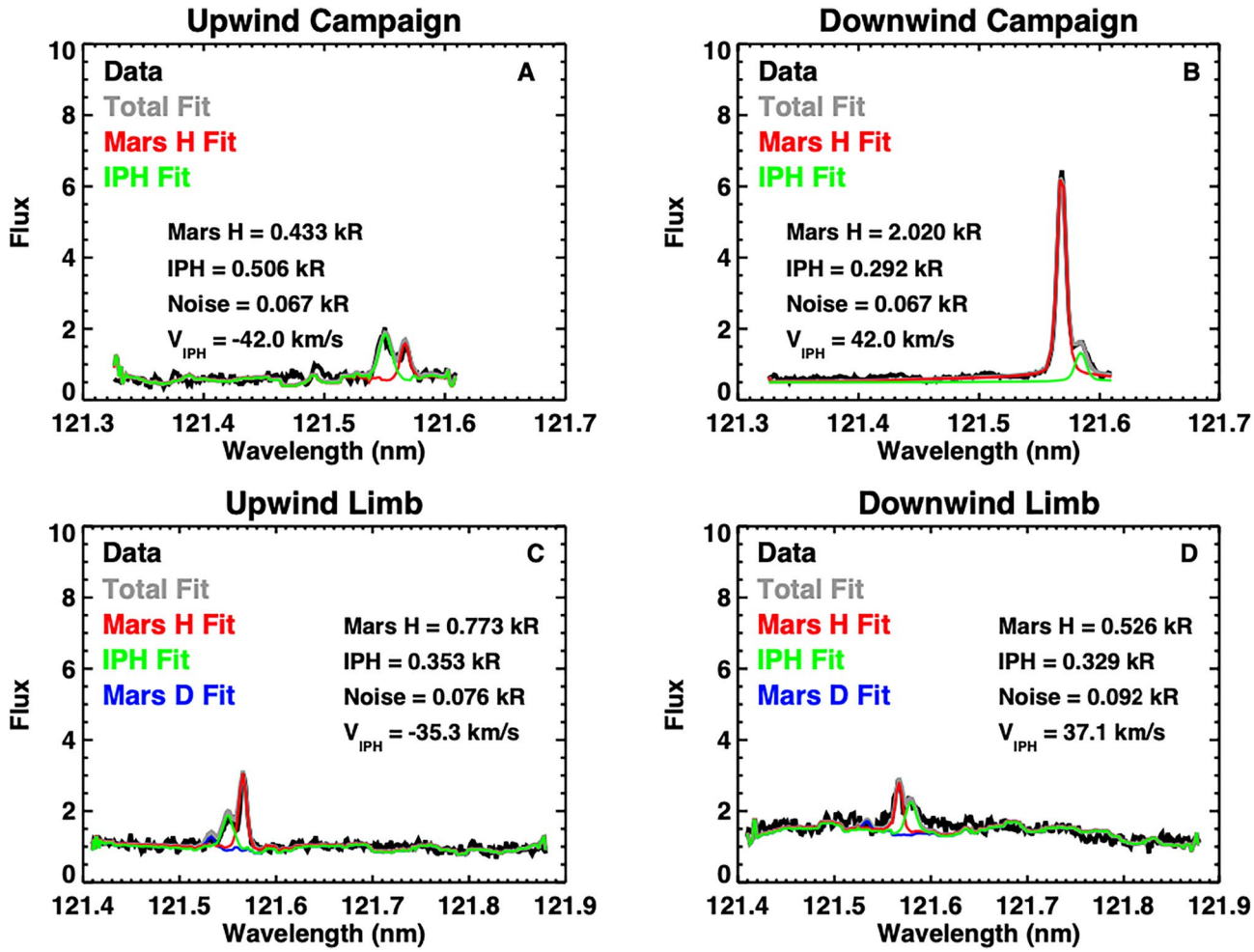

Figure 3. Sample MVN/IUVS/ECH data showing Lyman-α emissions from planetary H, IPH, and planetary D (for limb scans). (a) Upwind campaign observation for orbit 01992 taken on 8 October 2015, at 8:11:11.00 UTC, when Mars was at 52° Ls. The MAVEN spacecraft was 1.66 AU from the Sun. The instrument line of sight was pointed at 229° ecliptic longitude and 7.2° ecliptic latitude. (b) Downwind campaign observation for orbit 10730 taken on 15 January 2020, at 13:22:00.00 UTC, when Mars was at 136° Ls. The MAVEN spacecraft was 1.57 AU from the Sun. The instrument line of sight was pointed at 118° ecliptic longitude and 0.4° ecliptic latitude. (c) Upwind limb observation for orbit 09976 (during the outbound segment of the orbit) taken on 23 September 2019, at 21:56:37.00 UTC, when Mars was at 84° Ls. The MAVEN spacecraft was 1.66 AU from the Sun. The instrument line of sight was pointed at 245° ecliptic longitude and 41.1° ecliptic latitude. (d) Downwind limb observation for orbit 09976 (during the inbound segment of the orbit) taken on 23 September 2019, at 23:39:41.00 UTC. Same Ls and distance from the Sun as in (c), but the instrument line of sight was pointed at 47.8° ecliptic longitude and −25.4° ecliptic latitude. For all panels, the averaged spectrum (black) is used to iteratively obtain the best fits for the Mars H (red) and IPH (green). The limb scans that are pointed close to the planet include a Mars D (blue) emission that is too faint to resolve above the noise level in the campaign data. The total best fit curve (gray) sums the Lyman-α emissions as well as the detector background level. The Mars thermal H emission brightness, IPH brightness, background level, and IPH velocity are shown in the legends. See Table A1 for additional observational information.

an average of ∼14°. The upwind limb scan observations deviated between ∼11° and 53° from the upwind flow direction, with an average of ∼30°. The IPH downwind campaign observations deviated by anywhere between ∼37° and 46° of the downwind flow direction, with an average of ∼42°. The downwind limb scan observations deviated between ∼25° and 30° from the downwind flow direction, with an average of ∼28°. This spread in the line of sight from absolute upwind/downwind is helpful for determining trends in the IPH properties across the flow.

To date, observation of IPH properties from Mars' orbital location have been limited and made only with MAVEN/IUVS Echelle channel (e.g., Mayyasi, Clarke, Quémerais, et al., 2017), whereas observation of IPH properties from Earth's vicinity are relatively abundant as observed by IBEX, SOHO/SWAN, and Hubble Space Telescope (e.g., Galli et al., 2022; Baliukin et al., 2022, and references therein). The cavity region near the Sun, an area void of any IPH, can spatially vary and so, such observations from both Earth and Mars would serve as

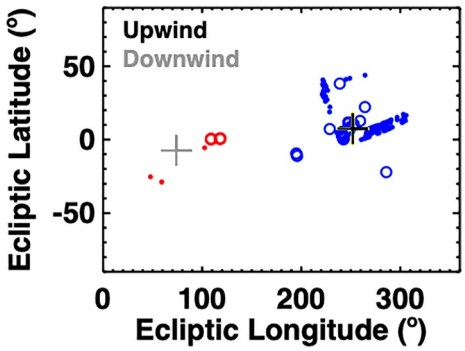

Figure 4. The distribution of observations relative to the upwind and downwind directions of the IPH flow, in ecliptic J2000 coordinates. Blue data points represent upwind observations made from IPH campaigns (open circles) and from limb scans (dots). Red data points represent downwind observations with similar symbols as used for upwind. The standard IPH upwind/downwind flow directions are shown as a black/gray crosses for reference.

useful constraints to inner heliospheric models of the IPH flow and its spatial variability where the simulation boundaries are assumed to be near 1–2 AU. The orbital distribution of the observations relative to the Sun and Earth are shown as a function of angle from upwind IPH flow in Figure 5.

The observations were predominantly made during aphelion when the relative Doppler from Mars was greatest. For upwind observations, the IPH campaign data points varied between 1.53 and 1.67 AU, with an average of 1.64 AU. For the upwind limb scans, the observations ranged between 1.56 and 1.66 AU with an average of 1.59 AU. For the downwind observations, the IPH campaign data points were at ∼1.57 AU. The downwind limb scans ranged between 1.58 and 1.67 AU with an average of 1.64 AU. During the aphelion season, Mars thermal H emissions are at their faintest, compared with the more turbulent dusty season at planet perihelion (Mayyasi et al., 2022a, 2022b). The data selection criteria and method for deriving IPH properties ensures that the IPH emission is as resolvable as possible from Mars' thermal emission. Further validation (described in Section 3 of the Results) confirms the independence of IPH properties from expected thermal H emission properties.

In the observations analyzed here, the Earth-Mars distance spanned 1.11–2.65 AU for upwind IPH campaign observations, with an average at 2.44 AU. The Earth-Mars distance for the limb-scan upwind data points ranged between 1.29 and 2.67 AU with an average of 1.72 AU. The downwind IPH campaign observations were all made at an Earth-Mars distance of 2.08 AU, and the downwind limb scan observations were at an Earth-Mars distance that ranged between 1.48 and 2.66 AU with an average of 2.26 AU. The IPH measurements made by MAVEN from Mars are not affected by terrestrial emissions, and Figure 5 demonstrates the additional constraints (relative to the Sun as well as Earth) that this data set provides compared with other data sets, such as those of SOHO/SWAN at L1.

4.2. Algorithmically Fit Properties

The IPH properties derived from the fitting algorithms are shown in Figure 6, as a function of angle from the upwind IPH flow. The IPH emission brightness was obtained by integrating the best fit emission line curve across wavelengths. The uncertainty in the brightness value calculated from each co-added spectrum was derived by examining a background region on the detector away from the emission region (Mayyasi, Clarke, Quémerais, et al., 2017; Mayyasi et al., 2023). The velocity was derived from the best fit Doppler shift to the IPH emission line peak, and the temperature was derived from the best fit value for the thermally broadened and convolved IPH emission line profile. It should be noted that the spectral resolution of the IUVS echelle spectra is not sufficient to accurately measure the IPH temperature, and in practice the assumed values in the fit are set to the expected range of temperatures from prior observations.

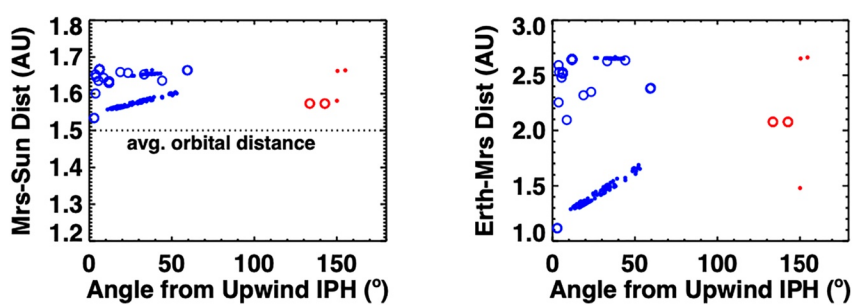

Figure 5. Orbital distance of the observations made at Mars relative to the Sun (Left) and to Earth (Right). Open circles are from IPH campaigns, small solid circles are from limb-scans. Blue data points correspond to upwind-oriented observations and red data points correspond to downwind-oriented observations.

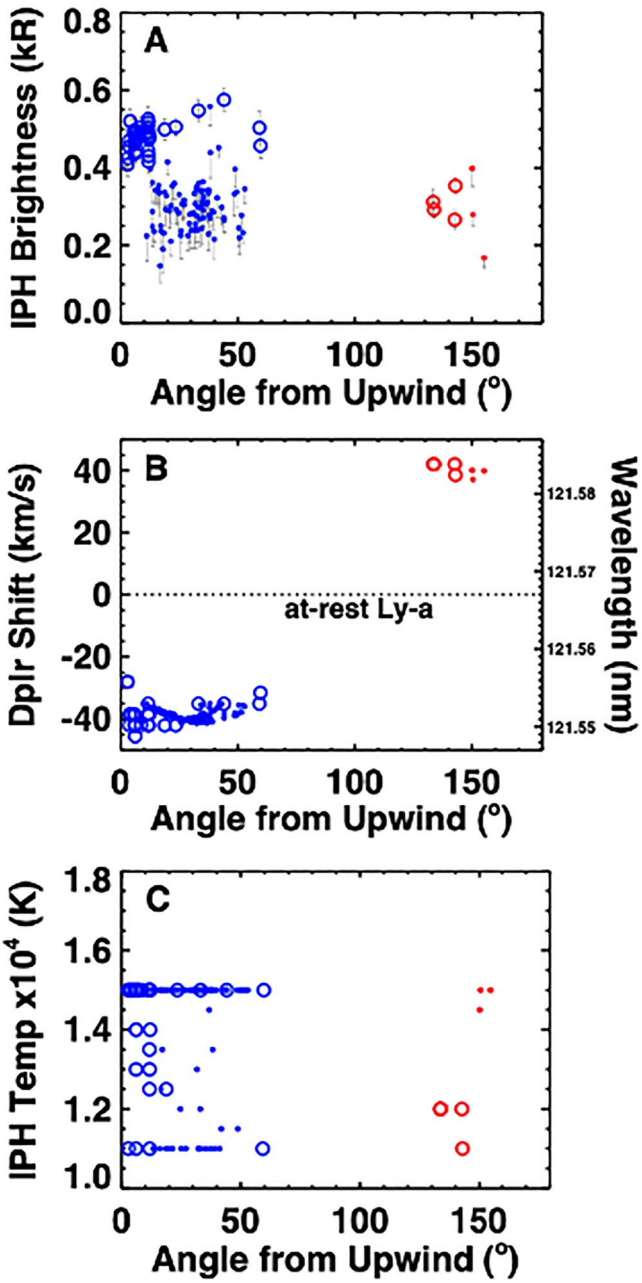

Figure 6. (a) The derived IPH brightness in kR, (b) Doppler shift in km/s and wavelength in nm, and (c) best-fit temperature in 10,000s K as a function of angle from the upwind IPH flow. The dashed line in panel (b) represents the at-rest Lyman-α Doppler shift (wavelength) of 0 km/s (121.567 nm). Unfilled circles represent properties derived from IPH campaigns. Smaller dots correspond to properties derived from limb scans. Blue symbols represent observations made upwind of the IPH flow and red symbols represent observations made downwind of the IPH flow.

In IPH campaign data, the line of sight is typically pointed away from Mars' disk, such that the IPH emission dominates the Lyman-α spectrum. Planetary thermal H emissions are removed. Additionally, non-thermal H atom emissions, that can contribute ∼15% of the total IPH signal, are detected and removed in the derivation of IPH brightness. In the limb data, the line of sight is much closer to the planet, resulting in a brighter Mars H thermal emission that renders any non-thermal Mars H components spectrally unresolvable from IPH emissions by the IUVS instrument. The IPH brightness derived from the limb data is therefore considered to be an upper limit and has been scaled down by 15% to account for any additional contribution from non-IPH atoms.

The resulting IPH brightness from upwind observing campaigns varied between 0.407 and 0.575 kR with an average of 0.478 kR. The IPH brightness in the upwind limb-oriented observations ranged between 0.147 and 0.558 kR with an average of 0.300 kR. The best fit IPH brightness in the downwind IPH campaign data ranged between 0.266 and 0.354 kR with an average of 0.306 kR. The best fit IPH brightness for the downwind oriented limb data ranged between 0.168 and 0.399 kR with an average of 0.282 kR. The uncertainties in the spectra varied for each data point, and ranged between 0.020 and 0.070 kR, with an average of 0.040 kR. Relative to the IPH emission, the uncertainties ranged between 4% and 26% with an average of 11%.

The IPH velocity is presented both as Doppler shift along the line of sight, in km/s, as well as in wavelength, relative to the at-rest Lyman-α line center. For upwind IPH campaign observations, the Doppler shift varied between −28.0 (−0.011) and −45.5 (−0.018) km/s (nm), with an average of −38.8 (−0.016) km/s (nm). For upwind limb scans, the Doppler shift varied between −35.0 (−0.014), as constrained for visibility, and −41.2 (−0.017) km/s (nm) with an average of −38.5 (−0.016) km/s (nm). For downwind IPH campaign observations, the Doppler shift varied between 38.5 (0.016) and 42.0 (0.017) km/s (nm) with an average of 41.2 (0.017) km/s (nm). For the downwind oriented limb scans, the Doppler shift varied between 37.1 (0.015) and 40.1 (0.016) km/s (nm) with an average of 39.0 (0.016) km/s (nm). These results are consistent with the first estimate predictions of Doppler shift derived from the line of sight observing geometry.

The best-fit temperature of the IPH flow covered the full range of fitting values and reached the preset boundary values (11,000–15,000 K) in most cases. For upwind IPH campaign observations, the fit temperatures averaged ∼14,100 K while the upwind limb scans averaged ∼14,400 K. The downwind IPH campaign observation best fit temperatures averaged of ∼11,800 K while the downwind limb scans averaged ∼12,000 K. However, the differences between these values are not significant due to the limited spectral resolution. Alternate boundaries were adopted in the fitting algorithm (10,000–28,000 K) and the results were similar in that the boundaries were reached for most of the data. The expanded thermal range did not affect the values of other fit properties (<1% for the brightness and 0% for the Doppler shift).

The campaign observation exposures are ∼1 hr in duration, with a line of sight that maintains the same RA and DEC for each frame and does not drift with the spacecraft. The limb observation exposures are ∼10 min in duration, with a line of sight that drifts minimally in RA and DEC. The maximum difference in spacecraft velocity between the book-end observations analyzed for the limb scans used in this work is between 0.1 km/s and 1.7 km/s for a given orbit used per data

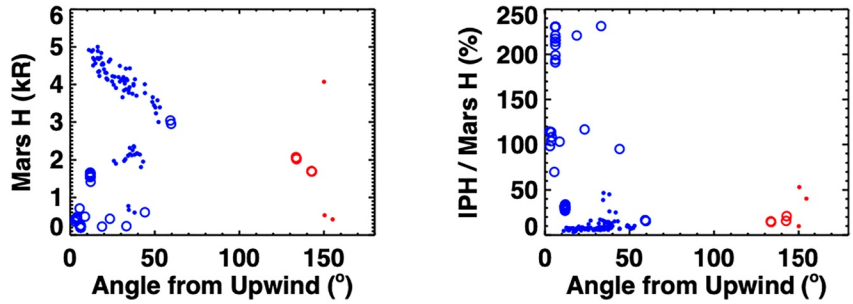

Figure 7. (Left) The best fit brightness of the thermal Martian H emissions as a function of IPH upwind flow angle. (Right) The percentage of IPH to Mars H brightness. Open circles indicate data observed during IPH campaigns. Dots indicate data obtained during limb scan observations. Blue data points indicate upwind observations. Red data points are obtained pointing downwind of the IPH flow.

point. With a spectral resolution of 0.0014 nm (~3.5 km/s), the compounded effects of line of sight pointing and spacecraft velocity shifts would not have an observable spectral broadening signature in the data.

The plotted spread in thermal values is not considered to be significant. The spectral resolution of the IUVS echelle spectra is not sufficient to resolve the expected temperature differences, and in practice the fitted values of IPH temperature are limited by the assigned limits to the range of temperature values. This suggests that improved spectral resolution and signal to noise would be needed for improved determinations of IPH emission line width.

4.3. Comparison to Planetary Emissions

The best fit Mars H emissions were integrated across wavelength to derive a planetary H brightness that is shown in Figure 7. Martian H atoms are generally thermalized within the collisional region of the upper atmosphere (Matta, 2013; Mayyasi et al., 2018, 2019b). During IPH campaigns, the line of sight was oriented tangentially to Mars or away from the planet, and so, the Mars H brightness was expected to be fainter than when the line of sight was directed toward the planet. The average Mars H brightness was verified to be lower during IPH campaigns and ranged between 0.198 and 3.00 kR with an average of 1.01 kR. In the limb-oriented observations, the Mars H brightness values were larger and ranged between 0.417 and 5.00 kR with an average of 3.57 kR.

Relative to the Mars H emission brightness, the IPH brightness can range between a significant or negligible component. For IPH campaign observations, the line of sight was optimized to capture IPH emissions, that can often exceed those from planetary H atoms and dominate the total Lyman-α spectral emission. Upwind IPH campaign observations showed the IPH contribution to vary between 15% and 231% with an average of 111%. The upwind limb observations showed the IPH contribution to vary between 4% and 55% with an average of 12%. In the downwind IPH campaign observations, the IPH contribution varied between 14% and 21% with an average of 17%. In the downwind limb scans, the IPH contribution ranged between 12% and 62% with an average of 40%.

To validate the results, a comparison of Mars H and IPH emission brightness was made over a range of solar illumination conditions along the line of sight, as shown in Figure 8. Variability in planetary H emissions is a

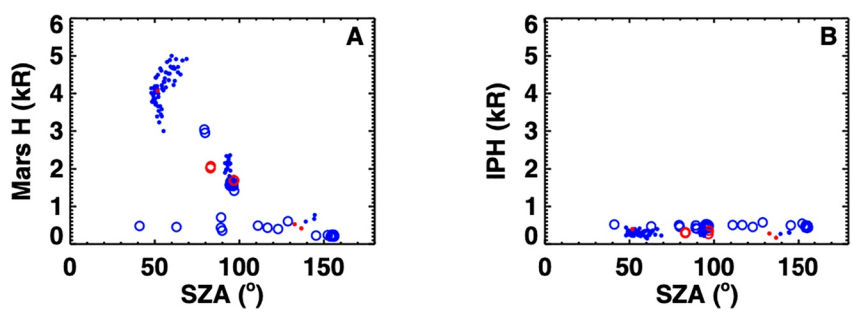

Figure 8. The variability of H emission brightness with solar illumination, denoted by solar zenith angle, derived from (a) Mars thermal atoms, and (b) Interplanetary atoms.

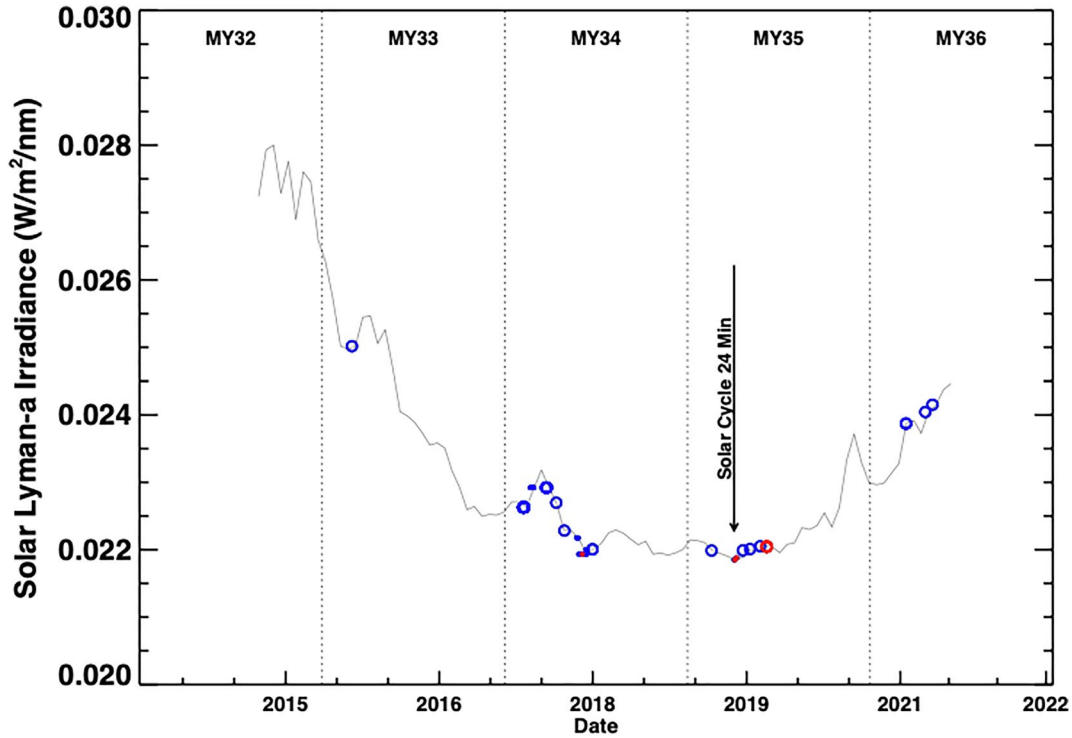

Figure 9. Sampling of IPH observations with time and solar activity, across the MAVEN mission timeline. The gray line shows the 28-day averaged Solar Lyman-α irradiance with symbols indicating the times of the IPH observations analyzed in this work. Blue and red open circles indicate IPH campaign observations oriented upwind and downwind to the IPH flow, respectively. Small blue and red circles indicate limb pointed observations made upwind and downwind to the IPH flow, respectively. Vertical black dotted lines separate MYs. An arrow indicates the minimum solar irradiance measurements, indicating the minimum activity period of Solar Cycle 24 (mid-September 2019).

consequence of multiple factors that include season, atmospheric dynamics, and observational geometry. The variation in brightness with illumination, denoted by solar zenith angle (SZA), of the tangent point to Mars along the line of sight demonstrated these effects. As expected, the Martian H brightness has a strong dependence on SZA and decreases with increasing SZA for the limb observations (Mayyasi et al., 2022a). During the campaign observations, the instrument LOS is pointed away from Mars and typically encounters a smaller (fainter) column of planetary H atoms. The IPH brightness did not show similar trends with SZA, as expected, for a source emission that is independent of fractional column illumination near Mars.

4.4. Solar Cycle Effects

The MAVEN/ECH observations utilized here included one data point in Mars Year (MY) 33, 107 data points in MY34, 13 datapoints in MY35, and 4 data points in MY36. During this timeline, solar activity was declining through Solar Cycle 24 into its minimum phase (~mid September 2019) through the rising activity phase of Solar Cycle 25. The Solar Lyman-α irradiance was obtained by the empirical model developed by Kretzschmar et al. (2018) that uses SOHO Solar Ultraviolet Measurement of Emitted Radiation instrument observations at Lyman-α center (Lemaire et al., 2015) with Lyman-α composite (Woods et al., 2000; Machol et al., 2019). The empirical model is found at https://lasp.colorado.edu/lisird/data/lyman_alpha_model_ssi/. The solar Lyman-α irradiance is averaged over a solar rotation cycle (28 days) and shown for reference in Figure 9.

Since the H Lyman-α emission is caused by resonant scattering of solar photons, solar irradiance variations can contribute to variations in the IPH brightness observations. These effects can be mitigated to allow for a more accurate comparison of upwind versus downwind IPH properties. To determine and remove the effects of variable solar activity on the derived IPH brightness, the Solar Irradiance was scaled to the MY33 single data point, as shown in Figure 10. Since many of the data points were obtained within a few days of each other, the IPH brightness was also averaged over 28-day spans, to account for solar rotation variations in orbits taken close in

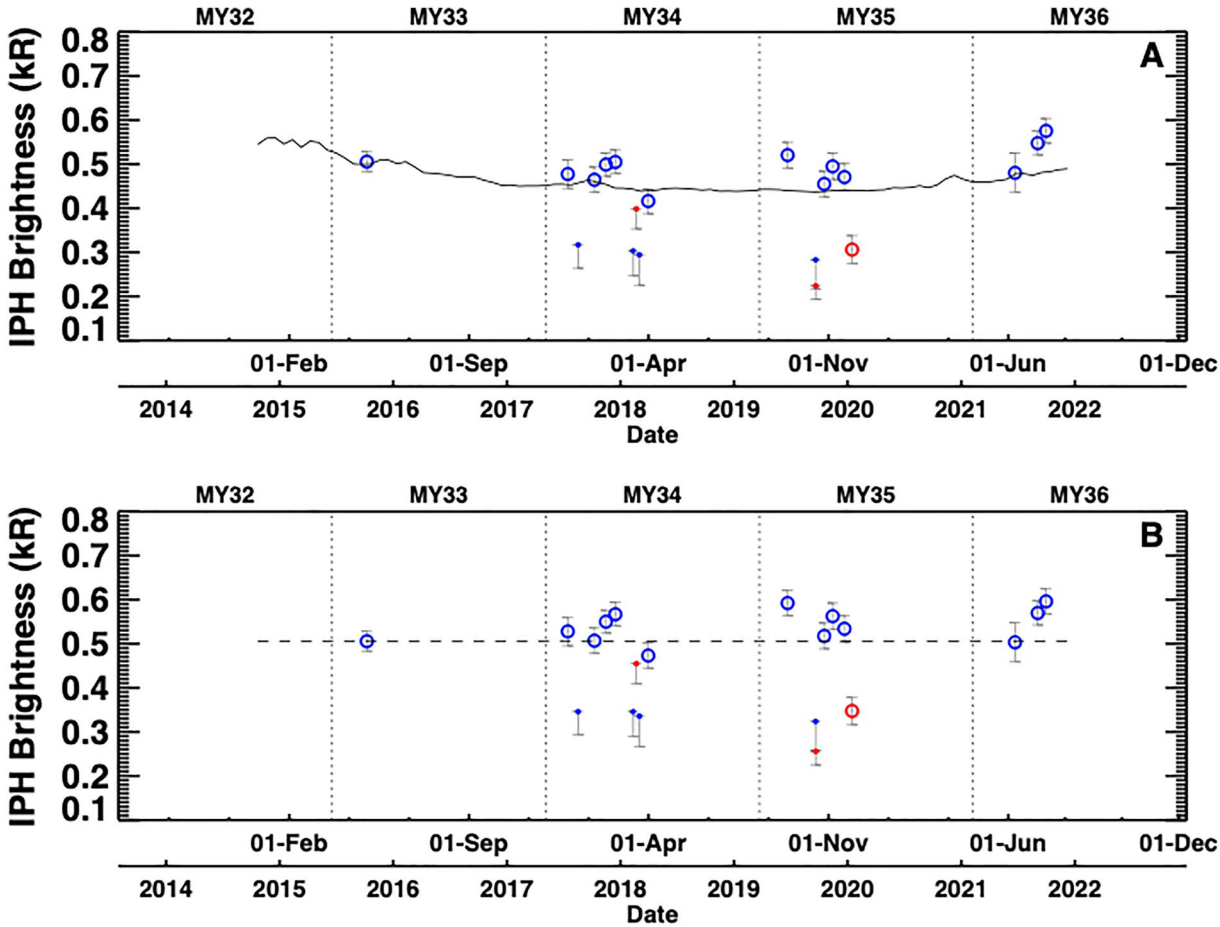

Figure 10. IPH brightness measurements with time, averaged over the 28 day solar rotation cycle. (a) The black line indicates the scaled solar Lyman-α irradiance, measured from Earth, also averaged over 28 days to account for solar rotation variations. (b) Same as Panel A but with the solar irradiance normalized (dashed black line) and with it the IPH brightness values to account for solar activity variations across the mission timeline.

time (as listed in Appendix A). The averaged IPH brightness followed the general trend of solar activity brightness with some scatter about the irradiance trendline. The IPH brightness was 0.506 kR for the single datapoint in MY33, and averaged 0.381 kR in MY34, 0.363 kR in MY35, and 0.520 kR in MY36, for data from each MY (from combined upwind, downwind, IPH campaign and limb-oriented data). The Solar Irradiance averaged 0.0240 W/m^2/nm in MY 33, 0.0220 W/m^2/nm in MY 34, 0.0220 W/m^2/nm in MY35, and 0.0237 W/m^2/nm in MY 36.

The data set includes a unique feature of having both upwind and downwind observations for IPH obtained around the same epoch in MY35, during Solar Cycle 24's minimum phase. Of the 13 observations available from that epoch, 7 were upwind and 6 were downwind. Four of the seven upwind observations were obtained during IPH campaigns, and three were obtained during limb-pointed scans. Additionally, four of the six downwind observations were obtained during IPH campaigns, and two were obtained during limb-pointed scans. To compare the upwind and downwind IPH properties, an adjustment to the data was implemented to normalize the effects of solar activity, that vary by ∼14%, for the available data set, between solar moderate conditions in MY33 to solar minimum conditions in MY35.

Solar irradiance variability was accounted for by constraining the brightness values to the irradiance in MY33 (at 0.025 W/m^2/nm) and normalizing the Solar irradiance for remaining data points to that value by adjusting the IPH brightness by a similar scaling factor as the irradiance normalization factor. The resulting correction is shown in Figure 10b. The normalized IPH brightness in MY33 remained unchanged and the averages for subsequent data points were 0.427 kR in MY34, 0.414 kR in MY35, and 0.543 kR in MY36.

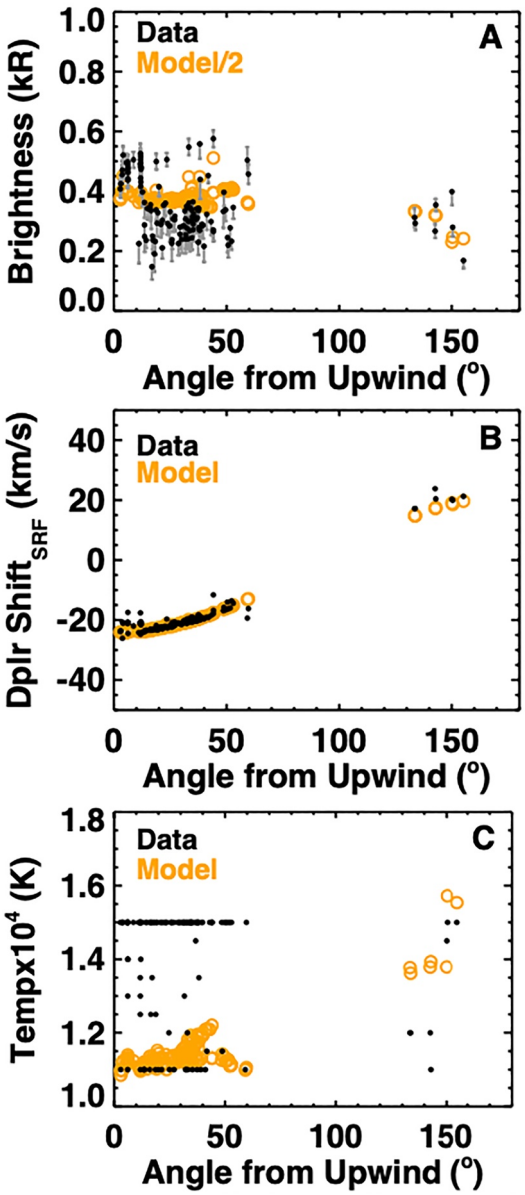

Figure 11. Data-model comparisons. Observations are shown as black dots and model values are show as yellow circles for all IPH data analyzed here (campaign and limb scans). Upwind observations are at angles less than 70° from upwind. Downwind observations are at angles larger than 130°. In panel (a) the observed brightness and its uncertainty (gray error bars) are compared to simulated values that have been scaled by a factor of 0.5. In panel (b), the Doppler shifts of observed and simulated values are shown in the solar rest frame (SRF). Panel (c) shows the temperatures obtained by the fits to the data as well as the model predictions.

Using the irradiance-normalized values, the average brightness, temperature, and Doppler shift of all upwind IPH observations from MY35 (campaign and limb-pointed) were 0.484 kR, 15000 K, and −37.7 km/s, respectively. The average brightness, temperature, and Doppler shift of all downwind observation from MY35 (campaign and limb-pointed) are 0.332 kR, 12800 K, and 40 km/s. While the Solar Cycle adjustments made to the IPH brightness values in MY35 at Solar Minimum changed minimally, this step is essential for a more complete analysis of the difference between upwind and downwind IPH properties and would have more significant impact when comparing data from other (past or future) more extreme solar epochs.

5. Interpretation

The IPH brightness showed that downwind H populations were fainter than the upwind populations. This was expected, as H atoms are more depleted closer to the Sun due to the combined effects of solar radiation pressure and photoionization with subsequent charge exchange that diminish their collective Lyman-α emissions (Bzowski et al., 2008; Sokół et al., 2019, 2020). These empirical results were consistent with previous findings (Clarke et al., 1995, 1998). When normalized to account for solar cycle variability, the values of solar irradiance and IPH brightness, averaged for each MY, correlated well (0.98 correlation coefficient) as would be causally expected for observations resulting from solar resonant scattering photons along a nearly constant column of IPH atoms.

The IPH velocity showed a decreasing trend as the line of sight moved away from up/downstream orientation toward cross-stream orientation, as was expected. The velocity scatter for similar viewing angle was due to the velocity of the MAVEN spacecraft. In Figure 11, the velocity is derived relative to the solar rest frame and demonstrates a smoother trend with angle from upwind/downwind flow, as expected.

The IPH temperature derivations were constrained to a range of values that are consistent with previous models and observations of IPH temperatures in the inner heliosphere (Costa et al., 1999; Quémerais, Lallement, Bertaux, et al., 2006). However, the best fits showed that the temperature range may have limited the fitting algorithm. A broader range of temperatures was applied, spanning 10,000–28,000 K, and showed the scatter in the best-fit temperatures to persist and to have minimal consequences on the brightness derivations that integrate across the spectral range. The absence of a smoother temperature trend is likely due to the data fitting algorithm that would result in very small changes in the χ^2 value for temperatures that are a few thousand K different paired with the limited spectral resolution of the data. Due to these factors, the derived temperatures should not be considered definitive.

In examining the relative contribution of IPH to the planetary emission from Mars' orbit, it was found that the IPH contribution ranged between significant (close to upwind orientations) and comparable (close to downwind orientation). This result is critical for lower-resolution Lyman-α observations made from Mars (and other planetary bodies with thermal H emissions) where assumptions are made to ignore IPH contributions or to assume a fixed value across a range of observing conditions.

6. Comparison to Model

IPH observations made in the inner heliosphere and relatively close to the Sun can serve to constrain heliospheric models due to the unique differences of flow properties along the various lines of sight in the region where photoionization, charge exchange with solar wind, solar gravity, and radiation pressure are dynamically affecting neutral H atoms. Additionally, the properties of interplanetary H atoms can be compared with models and observations of interplanetary He atoms for insights into the differences in flow dynamics throughout the heliosphere (e.g., Bzowski et al., 2019).

A heliospheric simulation tool was used to independently determine the brightness, Doppler shift, and temperature values of IPH atoms for the observations utilized here. The simulation used a 3-dimensional time-dependent kinetic-magnetohydrodynamic model that accounted for multi-constituent solar wind and interstellar plasmas, solar and interstellar magnetic fields, different hydrogen atom populations, and the latitudinal dependence of solar wind (Izmodenov & Alexashov, 2015, 2020). This global heliospheric model calculated the interstellar neutral H distribution at a sphere of radius 70 AU from the Sun as the boundary condition for a local model (Izmodenov et al., 2013; Katushkina et al., 2015).

The local model simulated the H distribution inside the 70-AU sphere by solving the kinetic equation to account for non-Maxwellian kinetic features, temporal variations of solar radiation pressure, and ionization rates during the solar cycle. Charge exchange ionization rates were taken from the analysis of the SOHO/SWAN Lyman-α observations (Katushkina et al., 2019; Koutroumpa et al., 2017) that were normalized using in situ data from the OMNIWeb database collected in the ecliptic plane (https://omniweb.gsfc.nasa.gov/). The dependence of radiation pressure on time, radial velocity, and heliolatitude of H atoms was adopted from Kowalska-Leszczynska et al. (2020). The total solar Lyman-α flux measured at the Earth's orbit was taken from Machol et al. (2019) (http://lasp.colorado.edu/lisird/data/composite_lyman_alpha/).

Using the H distribution from the model simulations, the solar Lyman-α radiation backscattered by H atoms was calculated. Single-scattered photon emissions were calculated by integrating the radiative transfer equation, and the multiple scattering emissions were calculated using the radiative transfer code developed by Quémerais (2000), which utilized the Monte Carlo method. In the simulations done for this work, the spectral properties that are moments of the Lyman-α spectrum were calculated. Namely, the brightness, line shift (Doppler shift), and line width (temperature) were obtained for the 125 observations made by MAVEN/IUVS.

The model brightness, Doppler shift, and temperature values were compared with the values derived from the observations, as shown in Figure 11. The simulated brightness values were consistently higher than the observed brightness values by a factor of two for both upwind and downwind datapoints. The comparison was therefore shown between the data and the modified simulated values (that were scaled by 0.5). This discrepancy may be in part due to differences between the model and data calibration methods (Mayyasi, Clarke, Quémerais, et al., 2017; Mayyasi et al., 2023; Baliukin et al., 2022), or may be due to the differences between the genuine distribution of H atoms in the heliosphere and that predicted in the model. At the time of this writing, upcoming HST/STIS observations of the upwind IPH are planned to occur simultaneously with MAVEN/IUVS observations (HST GO-Cycle 17196). Subsequent analysis of these data would help address any potential data/model calibration offsets.

The Doppler shifts, converted into the solar rest frame (SRF) were compared for the empirical and simulated results. These are found to be in good agreement for both upwind and downwind observations. This agreement verifies that the data derivation for IPH emission was accurate and consistent with model predictions of IPH flow direction and velocity.

The simulated temperatures were, on average, ∼20% cooler and showed less scatter than the average temperatures derived from the fits to the data. For the lines of sight simulated in this work, the resulting model temperatures ranged between ∼10,850 and 15,720 K as bounded by initial conditions. In the fits to the data, the temperatures ranged between 11,000 K and 15,000 K and were re-fit using temperatures that ranged between 10,000–28,000 K, all of which cover previous estimates of IPH flow temperatures. With both temperature ranges, the data-fitting algorithms did not compare well to the simulated values, likely due to the limited spectral resolution of the data, as discussed previously. The model predicts higher temperatures for downwind IPH atoms than for upwind atoms, as is consistent with previous estimates (Izmodenov, 2006; Katushkina & Izmodenov, 2011).

7. Summary

Data from the MAVEN IUVS Echelle channel were analyzed for derivation of IPH properties both upwind and downwind of the flow. The data set includes both dedicated campaign as well as fortuitous limb-pointed data upwind of the IPH flow, and serendipitous data downwind of the IPH flow from comet-pointed and limb-pointed data. The IPH emission brightness, Doppler shift, and thermal broadening were derived using a least square fitting algorithm. The resulting derivations showed trends of decreasing brightness with increasing angle from upwind. Independent model results showed similar trends and showed a consistent factor of two difference in brightness values. The data-model comparison also showed very good agreement with the derived and simulated velocities (Doppler shift). The temperature derivations in the data did not match the modeled values, likely due to limitations in the spectral resolution of the data.

The IPH brightness derived from the limb observations have more scatter and larger uncertainties than those derived from campaign observations. This is more statistically significant for downwind observations where there are three datapoints in the limb-pointed observations and four datapoints in the campaign (comet) observations. However, the scatter in derived velocities is much smaller in the limb data than in the campaign data. The temperature derivations are not considered optimal due to spectral resolution limitations in the instrument, yet for temperatures that were derived within the boundary values of the fitting algorithm, campaign datapoints yielded higher temperatures upwind than downwind, as expected.

In comparisons to the model, the brightness values derived from campaign versus limb data compared similarly with the simulated values. The velocity values from campaign versus limb data compared remarkably well with simulated values. The temperature derivations from both campaign and limb data were similarly divergent from simulated values. The results of the analysis and associated conclusions of this work do not change when using only the IPH campaign or limb datasets separately. We conclude that there is merit to analysis of both datasets in deriving IPH properties and expect more statistically significant trends to show with additional data obtained from future observations.

In summary, IPH atoms observed from Mars' vantage have provided constraints that show some agreements as well as disagreements with theoretical predictions. Understanding these differences will refine our understanding of how the IPH flow is affected by interface dynamics at the outer edge of the heliosphere as the flow propagates closer to the Sun. Ongoing IPH observing campaigns made with MAVEN/IUVS/Echelle would add valuable datapoints to this data set, especially when downwind observing opportunities arise to supplement the limited downwind data. These and future analyses can further elucidate how solar drivers affect heliospheric dynamics in the inner solar system.

Appendix A: Additional Details

A1. Observational Details

The observational data used in this analysis are listed in Table A1. Frames from each orbit were co-added to reduce the signal to noise. The total exposure time for the data in an orbit, used to derive a spectrum varies between 580 s for the limb scans (29 s each for 20 frames) to 3,600 s for the IPH/Comet campaign scans (60 s each for 60 frames).

Table A1
List of Observations Used in This Work. SC Represents the MAVEN Spacecraft

Mars year	SC orbit	Date	Time (UTC)	SC altitude (km)	SC speed (km/s)
Upwind Campaign					
33	1992	10/8/2015	8:11:11.00	6207	1.57
34	5398	7/13/2017	0:44:4.00	4294	2.16
	5402	7/13/2017	18:50:16.00	4289	2.16
	5404	7/14/2017	3:53:20.00	4287	2.16
	5406	7/14/2017	12:56:21.00	4286	2.16

Table A1
Continued

Mars year	SC orbit	Date	Time (UTC)	SC altitude (km)	SC speed (km/s)
	5410	7/15/2017	7:2:13.00	4295	2.16
	5412	7/15/2017	16:5:16.00	4293	2.16
	5414	7/16/2017	1:8:20.00	4289	2.16
	5416	7/16/2017	10:11:21.00	4288	2.16
	5418	7/16/2017	19:14:22.00	4289	2.16
	5420	7/17/2017	4:17:31.00	4291	2.16
	5422	7/17/2017	13:20:48.00	4291	2.16
	5866	10/8/2017	4:30:12.00	5977	1.60
	5868	10/8/2017	13:22:33.00	5977	1.60
	5869	10/8/2017	17:48:44.00	5977	1.60
	5870	10/8/2017	22:14:53.00	5976	1.60
	5871	10/9/2017	2:41:4.00	5977	1.60
	5872	10/9/2017	7:7:16.00	5976	1.60
	5873	10/9/2017	11:33:26.00	5974	1.60
	5874	10/9/2017	15:59:36.00	5976	1.60
	5875	10/9/2017	20:25:48.00	5975	1.60
	6074	11/15/2017	2:54:14.00	5815	1.63
	6241	12/15/2017	12:17:16.00	6052	1.60
	6806	3/30/2018	22:55:49.00	4216	2.17
	6808	3/31/2018	7:52:11.00	4214	2.17
35	9359	6/22/2019	5:28:1.00	4412	1.87
	10134	10/17/2019	19:10:58.00	4341	1.89
	10315	11/14/2019	1:33:13.00	4326	1.89
	10567	12/22/2019	0:9:14.00	4315	1.89
36	14212	6/21/2021	18:47:52.00	3143	2.36
	14220	6/22/2021	23:38:58.00	3145	2.36
	14701	9/3/2021	5:2:30.00	4239	1.92
	14880	9/30/2021	3:45:26.00	2666	2.59
Downwind Campaign (aka Comet)					
35	10728	1/15/2020	8:12:40.00	2437	2.69
	10730	1/15/2020	15:27:16.00	2433	2.69
	10728	1/15/2020	6:7:22.00	2566	2.63
	10730	1/15/2020	13:22:0.00	2570	2.62
Upwind Limb					
34	5398	7/13/2017	0:44:4.00	4294	2.16
	5402	7/13/2017	18:50:16.00	4289	2.16
	5404	7/14/2017	3:53:20.00	4287	2.16
	5406	7/14/2017	12:56:21.00	4286	2.16
	5410	7/15/2017	7:2:13.00	4295	2.16
	5412	7/15/2017	16:5:16.00	4293	2.16
	5414	7/16/2017	1:8:20.00	4289	2.16
	5416	7/16/2017	10:11:21.00	4288	2.16
	5418	7/16/2017	19:14:22.00	4289	2.16

Table A1
Continued

Mars year	SC orbit	Date	Time (UTC)	SC altitude (km)	SC speed (km/s)
	5420	7/17/2017	4:17:31.00	4291	2.16
	5422	7/17/2017	13:20:48.00	4291	2.16
	5544	8/9/2017	13:58:8.00	3148	2.57
	5544	8/9/2017	14:0:11.00	2998	2.63
	5570	8/14/2017	11:26:59.00	3438	2.46
	5570	8/14/2017	11:31:5.00	3149	2.57
	5582	8/16/2017	17:29:58.00	3453	2.45
	5582	8/16/2017	17:34:4.00	3165	2.56
	5582	8/16/2017	17:36:7.00	3016	2.62
	5590	8/18/2017	5:22:20.00	3440	2.45
	5596	8/19/2017	8:15:41.00	3141	2.56
	5596	8/19/2017	8:17:45.00	2991	2.62
	5602	8/20/2017	10:56:5.00	3441	2.45
	5602	8/20/2017	10:58:8.00	3300	2.50
	5602	8/20/2017	11:0:11.00	3155	2.56
	5602	8/20/2017	11:2:13.00	3008	2.61
	5608	8/21/2017	13:36:37.00	3426	2.45
	5608	8/21/2017	13:38:39.00	3286	2.5
	5608	8/21/2017	13:42:45.00	2993	2.62
	5866	10/8/2017	4:30:12.00	5977	1.60
	5868	10/8/2017	13:22:33.00	5977	1.60
	5869	10/8/2017	17:48:44.00	5977	1.60
	5870	10/8/2017	22:14:53.00	5976	1.60
	5871	10/9/2017	2:41:4.00	5977	1.60
	5872	10/9/2017	7:7:16.00	5976	1.60
	5873	10/9/2017	11:33:26.00	5974	1.60
	5874	10/9/2017	15:59:36.00	5976	1.60
	5875	10/9/2017	20:25:48.00	5975	1.60
	6074	11/15/2017	2:54:14.00	5815	1.63
	6241	12/15/2017	12:17:16.00	6052	1.60
	6486	1/30/2018	9:15:43.00	3389	2.47
	6500	2/1/2018	23:59:37.00	3397	2.47
	6500	2/2/2018	0:1:39.00	3256	2.52
	6504	2/2/2018	17:54:56.00	3396	2.47
	6504	2/2/2018	17:59:2.00	3109	2.58
	6516	2/4/2018	23:42:57.00	3246	2.52
	6516	2/4/2018	23:45:0.00	3101	2.58
	6530	2/7/2018	14:30:7.00	2954	2.64
	6550	2/11/2018	8:2:53.00	3097	2.58
	6554	2/12/2018	1:53:35.00	3389	2.47
	6562	2/13/2018	13:49:11.00	2963	2.63
	6566	2/14/2018	7:37:51.00	3399	2.47
	6574	2/15/2018	19:27:2.00	3417	2.46

Table A1
Continued

Mars year	SC orbit	Date	Time (UTC)	SC altitude (km)	SC speed (km/s)
	6584	2/17/2018	16:13:48.00	3409	2.46
	6584	2/17/2018	16:17:54.00	3121	2.57
	6588	2/18/2018	10:8:31.00	3405	2.46
	6588	2/18/2018	10:10:33.00	3264	2.52
	6592	2/19/2018	4:5:5.00	3265	2.52
	6592	2/19/2018	4:9:11.00	2971	2.63
	6596	2/19/2018	21:57:40.00	3405	2.46
	6596	2/19/2018	21:59:43.00	3263	2.52
	6596	2/19/2018	22:1:46.00	3118	2.57
	6596	2/19/2018	22:3:49.00	2969	2.63
	6602	2/21/2018	0:51:31.00	3264	2.52
	6602	2/20/2018	22:1:55.00	3373	2.48
	6606	2/21/2018	18:47:58.00	3123	2.57
	6610	2/22/2018	12:40:22.00	3271	2.51
	6610	2/22/2018	12:42:26.00	3125	2.57
	6610	2/22/2018	12:44:28.00	2977	2.63
	6806	3/30/2018	22:55:49.00	4216	2.17
	6808	3/31/2018	7:52:11.00	4214	2.17
35	9916	9/14/2019	20:2:41.00	3011	2.43
	9964	9/22/2019	2:24:24.00	3014	2.42
	9976	9/23/2019	21:56:37.00	3007	2.43
	9359	6/22/2019	5:28:1.00	4412	1.87
	10134	10/17/2019	19:10:58.00	4341	1.89
	10315	11/14/2019	1:33:13.00	4326	1.89
	10567	12/22/2019	0:9:14.00	4315	1.89
	10728	1/15/2020	8:12:40.00	2437	2.69
	10730	1/15/2020	15:27:16.00	2433	2.69
	10728	1/15/2020	6:7:22.00	2566	2.63
	10730	1/15/2020	13:22:0.00	2570	2.62
36	14212	6/21/2021	18:47:52.00	3143	2.36
	14220	6/22/2021	23:38:58.00	3145	2.36
	14701	9/3/2021	5:2:30.00	4239	1.92
	14880	9/30/2021	3:45:26.00	2666	2.59
Downwind Limb					
34	6602	2/20/2018	22:1:55.00	3373	2.48
35	9932	9/17/2019	7:53:56.00	3388	2.26
	9976	9/23/2019	23:39:41.00	3392	2.26

A2. Methodology Details

The methodology for deriving the best fit function to the data was done by minimum variance analysis. A curve was generated to best fit the emission spectrum using default settings for five parameters. The default settings were varied within expected ranges, described below, with each variation resulting in a different fit. Each fit was compared with the data, and the set of parameters that deviated the least from the data were used to generate the best fit.

The fitting parameters and their ranges are the spectral location (aka wavelength) of the Mars thermal emission peak (λ_{Mars}), the spectral location of the IPH emission peak (λ_{IPH}), the IPH temperature (T), the Mars H emission peak (f_{Mars}), relative to the total Mars emission at (λ_{Mars}), and the IPH emission peak (f_{IPH}), relative to the total IPH emission at (λ_{IPH}).

The five parameters and their ranges are:

- $\lambda_{Mars} = 121.567 \pm 0.2 \times$ FWHM nm, in 0.1 nm increments
- λ_{IPH} = derive from LOS ephemeris $\pm 0.2 \times$ FWHM nm, in 0.1 nm increments
- $T = 11{,}000$–$15{,}000$ K, in 500° increments
- $f_{Mars} = 100 \pm 10\%$, in 2% increments
- $f_{IPH} = 100 \pm 10\%$, in 2% increments

The total fit, Φ, was generated as follows:

$$\Phi = f_{Mars} \times \mathrm{LSF}_{Mars}(\lambda_{Mars}) + f_{IPH} \times \mathrm{LSF}_{IPH}(\lambda_{IPH}) \otimes \mathrm{Voigt}(T)$$

where LSF_{Mars} is the line spread function of the echelle instrument (Mayyasi et al., 2023). The LSF is used to generate a fit for the thermal Mars emission and is convolved with a thermally broadened Voigt profile to generate a fit for the IPH emission.

Once a fit was generated, the variance, χ^2, between the data and the fit was derived as follows:

$$\chi^2 = \left\{\Sigma_N[(\mathrm{data} - \Phi)^2. \times \mathrm{data}]\right\}/N$$

where N is the number of spectral elements.

The fitting algorithm loops through all values of λ_{Mars}, λ_{IPH}, T, f_{Mars}, and f_{IPH}. The set of values that produce the minimum χ^2 is selected and used to generate the best fit:

$$\Phi_{bestfit} = f_{Mars\_bestfit} \times \mathrm{LSF}_{Mars}(\lambda_{Mars\_bestfit}) + f_{IPH\_bestfit} \times \mathrm{LSF}_{IPH}(\lambda_{IPH\_bestfit}) \otimes \mathrm{Voigt}(T_{bestfit})$$

Data Availability Statement

The MAVEN limb data used in this study are available on the NASA PDS Atmospheres Node at https://pds-atmospheres.nmsu.edu/data_and_services/atmospheres_data/MAVEN/maven_main.html. IUVS echelle level1a data were used and reduced using the most up-to-date pipeline (Mayyasi et al., 2023).

Acknowledgments
This work was funded, in part, by NASA contract #1000320450 from the University of Colorado to Boston University. MM acknowledges the MAVEN mission for supporting the analysis of IUVS data. The MAVEN mission is supported by NASA in association with the University of Colorado and NASA's Goddard Space Flight Center. MM thanks the reviewers for their careful read of the manuscript and their helpful suggestions that helped improve the delivery of this work.

References

Baliukin, I. I., Bertaux, J.-L., Bzowski, M., Izmodenov, V. V., Lallement, R., Provornikova, E., & Quémerais, E. (2022). Backscattered solar Lyman-α emission as a tool for the heliospheric boundary exploration. *Space Science Reviews*, *218*(5), 45. https://doi.org/10.1007/s11214-022-00913-3

Bertaux, J. L., & Blamont, J. E. (1971). Evidence for a source of an extraterrestrial hydrogen Lyman-alpha emission. *Astronomy and Astrophysics*, *11*, 200–217.

Bertaux, J. L., Kyrölä, E., Quémerais, E., Pellinen, R., Lallement, R., Schmidt, W., et al. (1995). SWAN: A study of solar wind anisotropies on SOHO with Lyman alpha sky mapping. *Solar Physics*, *162*(1–2), 403–439. https://doi.org/10.1007/bf00733435

Bertaux, J. L., Lallement, R., Kurt, V., & Mironova, E. (1985). Characteristics of the local interstellar hydrogen determined from PROGNOZ 5 and 6 interplanetary Lyman α line profile measurements with a hydrogen absorption cell. *Astronomy and Astrophysics*, *150*, 1–20.

Bertaux, J. L., Quémerais, E., Lallement, R., Kyröelä, E., Schmidt, W., Summanen, T., et al. (1997). First results from SWAN Lyman a solar wind mapper on SOHO. *Solar Physics*, *175*(2), 737–770. https://doi.org/10.1023/a:1004979605559

Bzowski, M., Czechowski, A., Frisch, P., Fuselier, S., Galli, A., Grygorczuk, J., et al. (2019). Interstellar neutral helium in the heliosphere from IBEX observations. VI. The He+ density and the ionization state in the very local interstellar matter. *Appita Journal*, *882*(15), 60. https://doi.org/10.3847/1538-4357/ab3462

Bzowski, M., Möbius, E., Tarnopolski, S., Izmodenov, V., & Gloeckler, G. (2008). Diagnostics of interstellar hydrogen in the heliosphere Special feature Density of neutral interstellar hydrogen at the termination shock from Ulysses pickup ion observations. *A&A*, *491*(1), 7–19. https://doi.org/10.1051/0004-6361:20078810

Clarke, J., Lallement, R., Bertaux, J.-L., Fahr, H., Quémerais, E., & Scherer, H. (1998). HST/GHRS observations of the velocity structure of interplanetary hydrogen. *Appita Journal*, *499*(1), 482–488. https://doi.org/10.1086/305628

Clarke, J., Lallement, R., Bertaux, J.-L., Quémerais, E., & Scherer, H. (1995). HST/GHRS observations of the interplanetary medium downwind and in the inner solar system. *Appita Journal*, *448*, 893–904. https://doi.org/10.1086/176018

Costa, J., Lallement, R., Quémerais, E., Bertaux, J. L., Kyrölä, E., & Schmidt, W. (1999). Heliospheric interstellar H temperature from SOHO/SWAN H cell data. *Astronomy and Astrophysics*, *349*, 660–672.

Galli, A., Baliukin, I., Bzowski, M., Izmodenov, V., Kornbleuth, M., Kucharek, H., et al. (2022). The heliosphere and local interstellar medium from neutral atom observations at energies below 10 keV. *Space Science Reviews*, *218*(4), 31. https://doi.org/10.1007/s11214-022-00901-7

Izmodenov, V. (2007). Filtration of interstellar atoms through the heliospheric interface. *Space Science Reviews*, *130*(1–4), 377–387. https://doi.org/10.1007/s11214-007-9203-5

Izmodenov, V., & Alexashov, D. (2015). Three-dimensional kinetic-MHD model of the global heliosphere with the heliopause-surface fitting. *Astrophys. J. Suppl. Series, Special Issue*, *220*(2), 32. https://doi.org/10.1088/0067-0049/220/2/32

Izmodenov, V. V. (2006). In 'V. Izmodenov & R. kallenbach (Eds.), *ISSI scientific report´ No. 5* (pp. 45–64). *The physics of the heliospheric boundaries*. ESA-ESTEC.

Izmodenov, V. V., & Alexashov, D. B. (2020). Magnitude and direction of the local interstellar magnetic field inferred from Voyager 1 and 2 interstellar data and global heliospheric model. *Astronomy and Astrophysics*, *633*, L12. https://doi.org/10.1051/0004-6361/201937058

Izmodenov, V. V., Katushkina, O. A., Quémerais, E., & Bzowski, M. (2013). In E. 'Quémerais, M. Snow, & R.-M. Bonnet (Eds.), *ISSI scientific Report´ series*, *Cross-calibration of far-UV spectra of solar system objects and the heliosphere* (Vol. 13, p. 7). Springer-Verlag.

Jakosky, B., Lin, R. P., Grebowsky, J. M., Luhmann, J. G., Mitchell, D. F., Beutelschies, G., et al. (2015). The Mars atmosphere and volatile evolution (MAVEN) mission. *Space Science Reviews*, *195*(1–4), 3–48. https://doi.org/10.1007/s11214-015-0139-x

Katushkina, O., Galli, A., Izmodenov, V., & Alexashov, D. (2021). Analysis of the IBEX-Lo interstellar hydrogen fluxes collected in 2009–2018 as a tool for sensing of the solar radiation pressure and the hydrogen ionization rate. *MNRAS*, *501*(2), 1633–1643. https://doi.org/10.1093/mnras/staa3780

Katushkina, O., Izmodenov, V., Koutroumpa, D., Quémerais, E., & Jian, L. (2019). Unexpected behavior of the solar wind mass flux during solar maxima: Two peaks at middle heliolatitudes. *Solar Physics*, *294*(2), 17. https://doi.org/10.1007/s11207-018-1391-5

Katushkina, O. A., & Izmodenov, V. V. (2011). Spectral properties of the backscattered solar Ly-alpha radiation in the heliosphere: A theoretical search of the heliospheric boundaries effects. *Advances in Space Research*, *48*(12), 1967–1979. https://doi.org/10.1016/j.asr.2011.08.026

Katushkina, O. A., Izmodenov, V. V., & Alexashov, D. B. (2015). Direction of interstellar hydrogen flow in the heliosphere: Theoretical modelling and comparison with SOHO/SWAN data. *Monthly Notices of the Royal Astronomical Society*, *446*(3), 2929–2943. https://doi.org/10.1093/mnras/stu2218

Koutroumpa, D., Quémerais, E., Katushkina, O., Lallement, R., Bertaux, J. L., & Schmidt, W. (2017). Stability of the interstellar hydrogen inflow longitude from 20 years of SOHO/SWAN observations. *Astronomy and Astrophysics*, *598*, A12. https://doi.org/10.1051/0004-6361/201629840

Kowalska-Leszczynska, I., Bzowski, M., Kubiak, M. A., & Sokół, J. M. (2020). Update of the solar Lyα profile line model. *The Astrophysical Journal - Supplement Series*, *247*(2), 62. https://doi.org/10.3847/1538-4365/ab7b77

Kowalska-Leszczynska, I., Bzowski, M., Sokół, J., & Kubiak, M. (2018). Evolution of the solar lyα line profile during the solar cycle. II. How accurate is the present radiation pressure paradigm for interstellar neutral H in the heliosphere? *The Astrophysical Journal*, *868*(14pp), 49. https://doi.org/10.3847/1538-4357/aae70b

Kretzschmar, M., Snow, M., & Curdt, W. (2018). An empirical model of the variation of the solar Lyman-α spectral irradiance. *Geophysical Research Letters*, *45*(5), 2138–2144. https://doi.org/10.1002/2017GL076318

Lallement, R., Bertaux, J. L., & Clarke, J. T. (1993). Deceleration of interstellar hydrogen at the heliospheric interface. *Science*, *260*(5111), 1095–1098. https://doi.org/10.1126/science.260.5111.1095

Lallement, R., Quémerais, E., Bertaux, J. L., Ferron, S., Koutroumpa, D., & Pellinen, R. (2005). Deflection of the interstellar neutral hydrogen flow across the heliospheric interface. *Science*, *307*(5714), 1447–1449. https://doi.org/10.1126/science.1197340

Lallement, R., Quémerais, E., Koutroumpa, D., Bertaux, J. L., Ferron, S., Schmidt, W., & Lamy, P. (2010). The interstellar H flow: Updated analysis of SOHO/SWAN data. In (eds.), M. Maksimovic, K. Issautier, N. Meyer-Vernet, M. Moncuquet, & F. Pantellini (Eds.),. *Twelfth international solar wind conference*. *American institute of physics conference series*, (Vol. 1216, pp. 555–558). https://doi.org/10.1063/1.3395925

Lemaire, P., Vial, J.-C., Curdt, W., Schühle, U., & Wilhelm, K. (2015). Hydrogen Ly-α and Ly-β full Sun line profiles observed with SUMER/SOHO (1996–2009). *A&A*, *581*, A26. https://doi.org/10.1051/0004-6361/201526059

Machol, J., Snow, M., Woodraska, D., Woods, T., Viereck, R., & Coddington, O. (2019). An improved Lyman-alpha composite. *Earth and Space Science*, *6*(12), 2263–2272. https://doi.org/10.1029/2019EA000648

Matta, M. M. (2013). *Modeling the Martian ionosphere, PhD*. Boston University.

Mayyasi, M., Clarke, J., Bertaux, J.-L., Deighan, J., Bhattacharyya, D., Chaffin, M., et al. (2023). Upgrades to the MAVEN Echelle data reduction pipeline: New calibration standard and improved faint emission detection algorithm at Lyman-α. *Earth and Space Science*, *10*(4), e2022EA002602. https://doi.org/10.1029/2022EA002602

Mayyasi, M., Clarke, J., Bhattacharyya, D., Chaufray, J. Y., Benna, M., Mahaffy, P., et al. (2019a). Seasonal variability of deuterium in the upper atmosphere of Mars. *Journal of Geophysical Research: Space Physics*, *124*(3), 2152–2164. https://doi.org/10.1029/2018JA026244

Mayyasi, M., Clarke, J., Bhattacharyya, D., Deighan, J., Jain, S., Chaffin, M., et al. (2017). The variability of atmospheric deuterium brightness at Mars: Evidence for seasonal dependence. *Journal of Geophysical Research: Space Physics*, *122*(10), 10811–10823. https://doi.org/10.1002/2017JA024666

Mayyasi, M., Clarke, J., Chaufray, J.-Y., Kass, D., Bougher, S., Bhattacharyya, D., et al. (2022a). Solar cycle and seasonal variability of H in the upper atmosphere of Mars. *Icarus*, *393*, 115293. https://doi.org/10.1016/j.icarus.2022.115293

Mayyasi, M., Clarke, J., Chaufray, J. Y., Kass, D., Bougher, S., Bhattacharyya, D., et al. (2022c). Solar cycle and seasonal variability of H in the upper atmosphere of Mars. *Icarus*, *393*, 115293. https://doi.org/10.1016/j.icarus.2022.115293

Mayyasi, M., Clarke, J., Deighan, J., Jain, S., Chaffin, M., & Schneider, N. (2022b). The observed properties of H in the upper atmosphere of Mars. *AGU fall meeting 2022*. P42F-2472.

Mayyasi, M., Clarke, J., Quémerais, E., Katushkina, O., Bhattacharyya, D., Chaufray, J., et al. (2017). IUVS echelle-mode observations of interplanetary hydrogen: Standard for calibration and reference for cavity variations between Earth and Mars during MAVEN cruise. *Journal of Geophysical Research: Space Physics*, *122*(2), 2089–2105. https://doi.org/10.1002/2016JA023466

Mayyasi, M., Narvaez, C., Benna, M., Elrod, M., & Mahaffy, P. (2019b). Ion-neutral coupling in the upper atmosphere of Mars: A dominant driver of topside ionospheric structure. *Journal of Geophysical Research: Space Physics*, *124*(5), 3786–3798. https://doi.org/10.1029/2019JA026481

Mayyasi, M., Withers, P., & Fallows, K. (2018). A sporadic topside layer in the ionosphere of Mars from analysis of MGS radio occultation data. *Journal of Geophysical Research: Space Physics*, *123*(1), 883–900. https://doi.org/10.1002/2017JA024938

McClintock, W., Schneider, N. M., Holsclaw, G. M., Clarke, J. T., Hoskins, A. C., Stewart, I., et al. (2014). The imaging ultraviolet spectrograph (IUVS) for the MAVEN mission. *Space Science Reviews*, *195*(1–4), 75–124. https://doi.org/10.1007/s11214-014-0098-7

McComas, D. J., Schwadron, N. A., Crary, F. J., Elliott, H. A., Young, D. T., Gosling, J. T., et al. (2004). The interstellar hydrogen shadow: Observations of interstellar pickup ions beyond Jupiter. *Journal of Geophysical Research*, *109*(A2), A02104. https://doi.org/10.1029/2003JA010217

Quémerais, E. (2000). Angle dependent partial frequency redistribution in the interplanetary medium at Lyman α. *Astronomy and Astrophysics*, *358*, 353–367.

Quémerais, E., Bertaux, J.-L., Lallement, R., Berthé, M., Kyrölä, E., & Schmidt, W. (1999). Interplanetary Lyman α line profiles derived from SWAN/SOHO hydrogen cell measurements: Full-sky Velocity Field. *Journal of Geophysical Research*, *104*(A6), 12585–12603. https://doi.org/10.1029/1998ja900101

Quémerais, E., Lallement, R., Bertaux, J.-L., Koutroumpa, D., Clarke, J., Kyrölä, E., & Schmidt, W. (2006). Interplanetary Lyman-α line profiles: Variations with solar activity cycle. *Astronomy and Astrophysics*, *445*(3), 1135–1142. https://doi.org/10.1051/0004-6361:20065169

Quémerais, E., Lallement, R., Ferron, S., Koutroumpa, D., Bertaux, J.-L., Kyrölä, E., & Schmidt, W. (2006). Interplanetary hydrogen absolute ionization rates: Retrieving the solar wind mass flux latitude and cycle dependence with SWAN/SOHO maps. *Journal of Geophysical Research*, *111*(A9), A09114. https://doi.org/10.1029/2006JA011711

Quémerais, E., McClintock, B., Holsclaw, G., Katushkina, O., & Izmodenov, V. (2014). Hydrogen atoms in the inner heliosphere: SWAN-SOHO and MASCS-MESSENGER observations. *Journal of Geophysical Research: Space Physics*, *119*(10), 8017–8029. https://doi.org/10.1002/2014JA019761

Rodríguez Moreno, D., Wurz, P., Saul, L., Bzowski, M., Kubiak, M., Sokół, J., et al. (2013). Evidence of direct detection of interstellar deuterium in the local interstellar medium by IBEX. *A&A*, *557*, A125. https://doi.org/10.1051/004-6361/201321420

Sokół, J., Bzowski, M., & Tokumaru, M. (2019). Interstellar neutral gas species and their pickup ions inside the heliospheric termination shock. Ionization rates for H, O, Ne, and He. *The Astrophysical Journal*, *872*(1), 57. https://doi.org/10.3847/1538-4357/aafdaf

Sokół, J., McComas, D., Bzowski, M., & Tokumaru, M. (2020). Sun–heliosphere observation-based ionization rates model. *The Astrophysical Journal*, *897*(2), 179. https://doi.org/10.3847/1538-4357/ab99a4

Solomon, P., & Woolf, J. (1973). Interstellar deuterium: Chemical fractionation. *Appita Journal*, *224*(1), 301–305. https://doi.org/10.1111/j.1749-6632.1973.tb41469.x

Thomas, G., & Krassa, R. (1971). OGO 5 measurements of the Lyman Alpha sky background. *Astronomy and Astrophysics*, *11*, 218.

Vincent, F., Ben-Jaffel, L., & Harris, W. (2011). Updated analysis of the upwind interplanetary hydrogen velocity as observed by the Hubble Space telescope during solar cycle 23. *The Astrophysical Journal*, *738*(2), 135. https://doi.org/10.1088/0004-637X/738/2/135

Vincent, F. E., Katushkina, O. A., Ben-Jaffel, L., Harris, W. M., Izmodenov, V., Quémerais, E., et al. (2014). Observations of the interplanetary hydrogen during solar cycle 23 and 24. What can we deduce about the local interstellar medium? *The Astrophysical Journal Letters*, *788*(2), L25. https://doi.org/10.1088/2041-8205/788/2/l25

Woods, T., Tobiska, K., Rottman, G., & Worden, J. (2000). Improved solar Lyman irradiance modeling from 1947 through 1999 based on UARS observations. *Journal of Geophysical Research*, *105*(A12), 27195–27215. https://doi.org/10.1029/2000ja000051

Wu, F., & Judge, D. (1980). A reanalysis of the observed interplanetary hydrogen Lα emission profiles and the derived local interstellar gas temperature and velocity. *Appita Journal*, *239*, 389–394. https://doi.org/10.1086/158119

Zank, G., Sterken, V., Giacalone, J., Möbius, E., von Steiger, R., Stone, E., et al. (2022). The early history of heliospheric science and the spacecraft that made it possible. *Space Science Reviews*, *218*(4), 34. https://doi.org/10.1007/s11214-022-00900-8